Proceedings of the Estonian Academy of Sciences,
2024, **73**, 4, 396–415
https://doi.org/10.3176/proc.2024.4.08
Available online at www.eap.ee/proceedings

APPLIED POWER ELECTRONICS

Comparative feasibility study of partial power converter for interfacing battery energy storage into power system of future circular collider

Andrii Chub[a*], Joosep Niinemägi[a,b], Manuel Colmenero[b] and Davide Aguglia[b]

[a] Department of Electrical Power Engineering and Mechatronics, Tallinn University of Technology, Ehitajate tee 5, 19086 Tallinn, Estonia
[b] Electrical Power Converter Group, CERN – European Organization for Nuclear Research, Geneva 23, Switzerland

Received 20 February 2024, accepted 16 October 2024, available online 19 November 2024

Abstract. The recent appearance of partial power converters has shown their potential to significantly improve the efficiency and power density of power electronic systems. However, their feasibility in different applications is not sufficiently studied. This paper examines a partial power converter based on the dual active bridge topology regarding its feasibility and performance for battery integration into the cells of a modular multilevel converter that feeds particle accelerator magnets. The simulation results prove that the given partial power converter can reject grid-frequency ripple on the battery side and control current with sufficient dynamics. Its comparison with typical DC-DC topologies reveals its acceptable cost, high efficiency, and power density. The findings are based on the numerical simulation in the MATLAB/Simulink environment and virtual prototyping based on available off-the-shelf components.

Keywords: power electronics, DC-DC converter, energy conversion efficiency, power density, particle accelerator.

1. INTRODUCTION

Power electronics is an enabling technology for many applications. Among them, particle accelerators present one of the most challenging niche applications. Exploring the nature of the matter, electron-hadron colliders were proposed and implemented [1]. Among these efforts is the ongoing feasibility study of the Future Circular Collider (FCC), which aims to achieve 100 TeV collision energy levels [2–4]. The proposed scale of the FCC yields a circumference of 90 km, overshadowing the existing Large Hadron Collider with a circumference of 27 km.

High power requirements, reaching hundreds of MW for the electron-positron collider (FCC-ee) stage and increasing further for the proton-proton collider (FCC-hh) stage, along with the need for considerably longer power supply feeders, necessitate a feasibility analysis of new energy distribution approaches [3,5]. One of the most challenging applications in the FCC is feeding high-power pulsed loads, such as accelerator magnets, due to the inherently cyclic operation of the accelerator [6,7]. Such a high peak power consumption could be satisfied by embedded battery energy storage to minimize energy losses in the distribution system and avoid high fluctuation of power consumption from the utility grid [5,8,9]. Moreover, having numerous on-site buildings and a vast territory occupied by facilities, CERN has good opportunities to offset the carbon footprint of the research infrastructure [10,11].

* Corresponding author, andrii.chub@taltech.ee

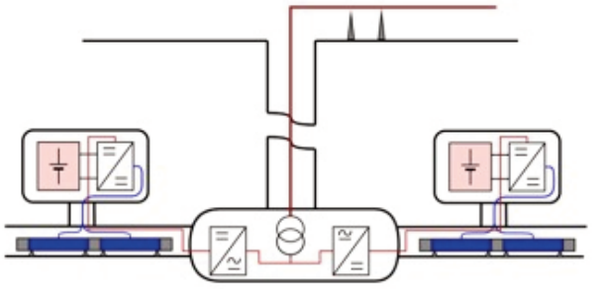

Fig. 1. Battery energy storage collocated with the accelerator magnets in caverns.

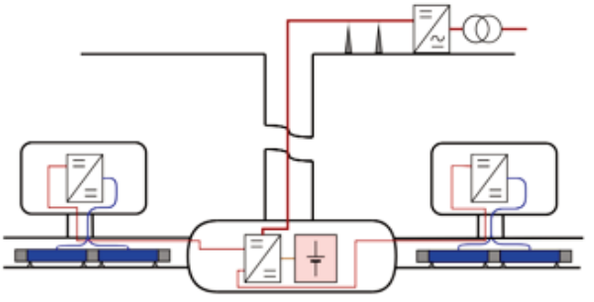

Fig. 2. Centralized battery energy storage.

Medium voltage DC (MVDC) is currently considered for energy distribution in the FCC to achieve higher efficiency and power quality [12]. It was conceptualized that MVDC can significantly improve the overall efficiency and power quality of the particle accelerator's power distribution system [9,12]. This technology inherently has no reactive power and harmonics issues, while it provides higher power transmission capabilities using similarly sized cables and simplifies energy recovery from accelerator magnets [13].

Numerous multilevel converters have been proposed for MVDC applications [14]. Among them, the modular multilevel converters (MMCs) were found to be the most suitable for AC grid interfacing of high-power loads in the FCC [15]. In addition, they provide excellent fault-tolerant features and allow for integrating the energy storage units at the submodule levels [9,16]. Since every arm of the MMC operates as a single-phase converter at the grid fundamental frequency, submodule capacitors exhibit sizable AC voltage ripple [17,18]. Consequently, battery integration requires an interfacing DC-DC converter capable of rejecting this voltage ripple and stabilizing the battery current [19]. On the other hand, it enables feeding and recovering energy from the accelerator magnets without causing disturbances in the AC grid. During the ongoing feasibility study, the lithium-titanate-oxide (LTO) batteries were selected as the main solution for use in the FCC due to their high safety and long lifetime [20]. The main benefits of using this battery type are high chemical stability and fire safety, along with low degradation per charge/discharge cycle [20,21]. This makes them ideal for FCC applications, such as capturing and releasing the energy of the accelerator's super-conductive magnets, where all other battery types cannot provide such a high number of charge/discharge cycles within their useful lifetime, while simplifying fire safety requirements for underground installations.

There are several possible approaches to energy storage integration in the FCC power system. Using batteries right next to the accelerator magnets, as shown in Fig. 1, minimizes losses when cycling energy between magnets and the corresponding battery energy storage. On the one hand, it requires the highest capital investments in digging caverns that can accommodate battery energy storage cabinets and the associated equipment for energy conversion and fire safety assurance. On the other hand, this approach is not practical for integration with the MVDC grid. Hence, alternative architectures have been considered.

The centralized energy storage allocation alongside the MVDC interface converter reduces capital investment and simplifies the maintenance of the battery packs. However, the distance between magnets and the battery energy storage increases, causing higher losses in wires. This issue could be alleviated if both the MMC and batteries were installed in dedicated locations in the caverns, as Fig. 2 shows. This approach is still associated with more bedrock removal, but capital costs could be reduced by minimizing the number of such locations across the FCC circumference.

Combining these two approaches could be implemented by distributing battery energy storage between the central MVDC interface converter installed on the surface level and local MVDC converters feeding accelerator coils installed in the caverns, as shown in Fig. 3. This approach optimizes expenses on bedrock removal to build caverns. Also, the total storage capacity is utilized during peak power demands, when the current in magnets is rumped up, while the local small storage improves efficient regulation of the magnet currents. This architecture can fully utilize MMC technology as a front-end converter that interfaces the

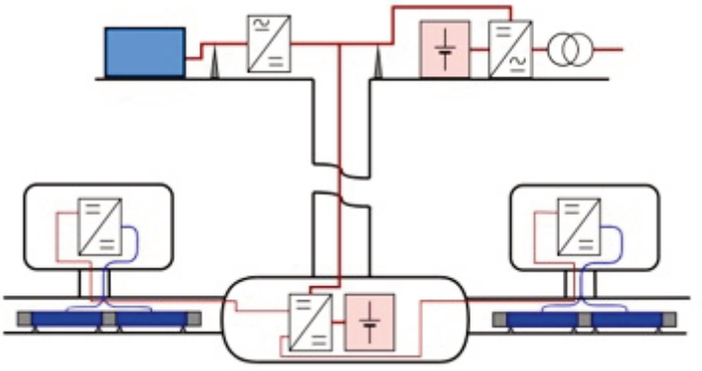

Fig. 3. Distributed battery energy storage based on MVDC power distribution, which has connection possibility to surface infrastructure.

MVDC grid with the AC distribution grid, while embedding the largest section of the distributed battery energy storage.

Battery integration into MMC submodules (SMs) has been under study for over a decade to reduce the cost of MVDC battery integration [19,22]. On the other hand, most of the research was concentrated on control challenges arising from this concept and utilized only generic bidirectional DC-DC converter topologies, such as non-isolated half-bridge or dual active bridge (DAB) converters [23–26]. In conventional applications, the power density of the converters is of little importance due to the large size of such converters associated with high creepage requirements. In the case of the given FCC application, the DC-DC converter's cost, efficiency, and size are paramount due to the costs associated with bedrock removal and the running costs directly associated with the efficiency of the electric power supply system. Hence, the FCC feasibility study must include an analysis of the existing and emerging DC-DC converters suitable for battery energy storage system (ESS) integration into MMC submodules, as illustrated in Fig. 4.

This paper proposes using a partial power converter (PPC) for battery ESS integration into an MMC submodule, which has not been demonstrated in the literature before. Such a converter utilizes a typically isolated DC-DC cell that processes only a fraction of the total power by regulating the voltage difference between its two ports [27–30]. As a result, most of the power is delivered without processing in a nearly lossless way. This allows for achieving much higher efficiency even if the efficiency of the DC-DC cell is mediocre, allowing for the utilization of low-cost off-the-shelf components [31,32]. This paper presents a PPC based on the DAB topology and benchmarks it against the two conventional solutions: a non-isolated half-bridge buck/boost DC-DC converter and a DAB converter, which were previously commonly used for battery ESS interfacing into an MMC submodule [23–26]. Therefore, three converters were implemented in MATLAB/Simulink to study their electrical parameters and facilitate practical design. It is worth noting that DAB-based PPCs have been explored before for different applications, such as electric vehicle battery charging, battery ESS interfacing, or power flow control in DC microgrids [33–38]. However, none of the available studies have demonstrated the ability of these PPCs to reject the grid-frequency voltage/current ripple. Such functionality typically requires a specialized control [39,40] or an integral solution combining control approaches with auxiliary circuits [41,42]. The literature demonstrates that typical controllers with a resonant component, such as the proportional-integral-resonant (PIR) controller, offer simple implementation and high ripple rejection performance in DC-DC applications [43] and, more specifically, in MMC submodule-level applications [42,44].

The following section presents the proposed converter and the baseline topologies used for comparison. The third section provides simulation results. The fourth section presents the results of virtual prototyping and a systematic comparison of the proposed and conventional converters regarding power losses, efficiency, volume, and cost of the components. The conclusions are provided at the end of the article.

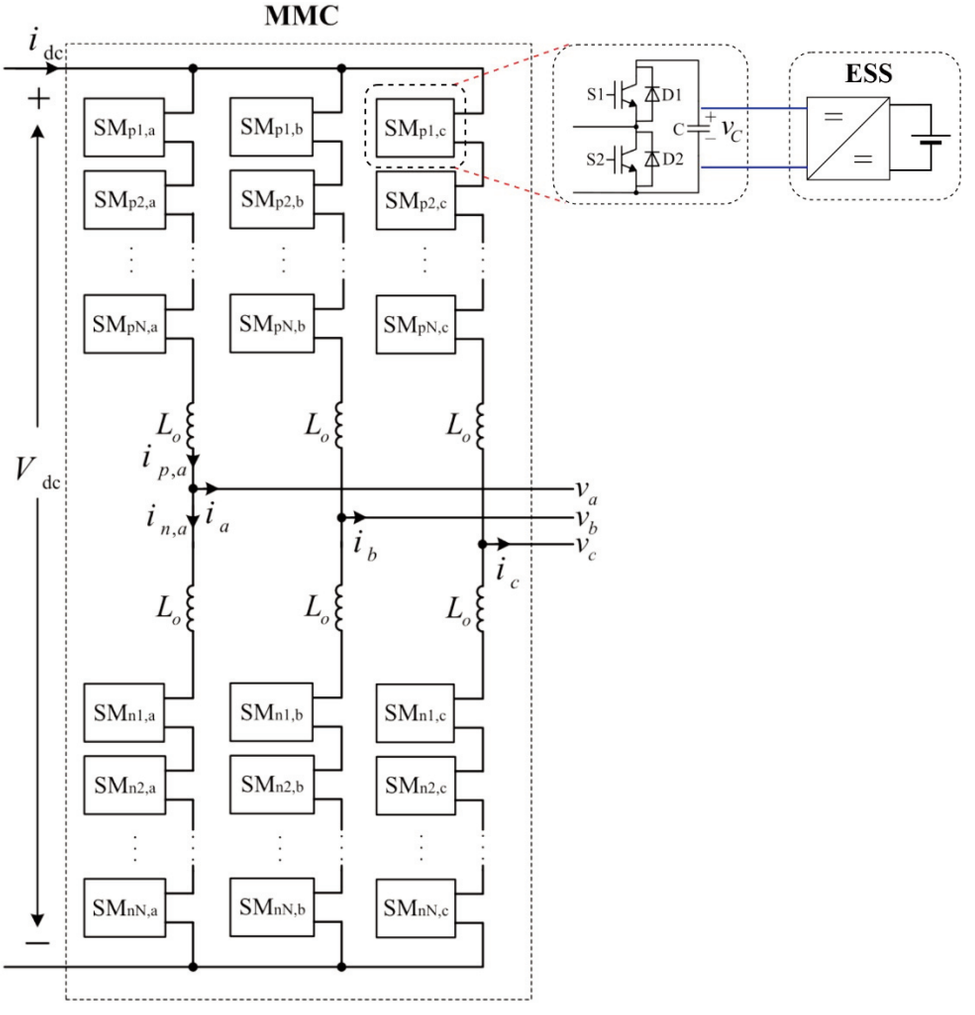

Fig. 4. Schematic of a typical MMC topology illustrating battery ESS integration into a submodule [26].

2. DESCRIPTION OF THE CASE STUDY CONVERTERS

As mentioned before, this study considers three bidirectional DC-DC converters, two conventional and one emerging, to evaluate which one can satisfy the requirements regarding low cost, high power density, and efficiency.

2.1. Conventional half-bridge buck/boost converter

The half-bridge buck/boost converter (Fig. 5) is a well-known bidirectional topology often used for its simplicity, high efficiency, low cost, and good voltage regulation capabilities. It employs a pair of power semiconductor switches arranged in a half-bridge configuration, with filtering capacitors and an inductor. Complementary control of the switches allows for avoiding discontinuous conduction mode in this topology, even at a zero average inductor current. As a result, they were found suitable for the integration of batteries into an MMC submodule [45].

Typical pulse-width modulation (PWM), when S_2 is controlled with the duty cycle of D and S_1 with a duty cycle of slightly less than 1–D, defines the converter gain as in (1). This characteristic is virtually

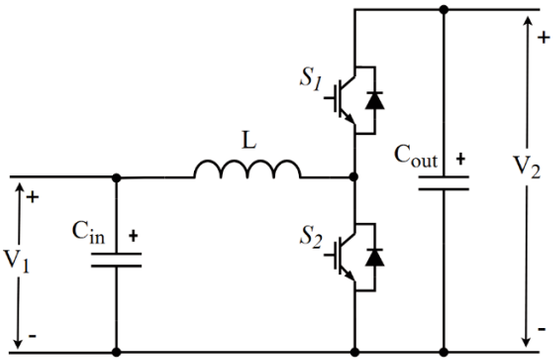

Fig. 5. Topology of the half-bridge converter.

independent of the load current, slightly influenced only by the voltage drop on the equivalent parasitic resistances (ESRs) of the converter components.

On the one hand, this topology can smoothly control the current and change the power flow control by adjusting only one control variable (*D*). On the other hand, the dynamic range of the control variable is limited as the inductor current value and its direction cause a minor voltage drop on the parasitic ESRs, which is compensated by small variations of the control variable *D*. This issue will be more evident from the simulation results in the next section.

$$G_{HB} = \frac{V_2}{V_1} = \frac{1}{1-D} \tag{1}$$

2.2. Conventional DAB converter

The DAB topology is commonly used in applications with desired galvanic isolation and wide input voltage regulation range [46]. Also, they have been applied for the integration of photovoltaic strings as well as battery packs in the MMC submodules to avoid issues with insulation and grounding of such systems, but at a premium cost of a bidirectional isolated DC-DC converter [47]. As this solution is among the most commonly used ones in the literature, it was selected as the second baseline topology for comparison with the emerging PPC.

This study utilizes the simplest modulation of the DAB converter (Fig. 6), referred to as the single phase shift control [48]. It requires the diagonal transistors of each active bridge to be controlled complementarily

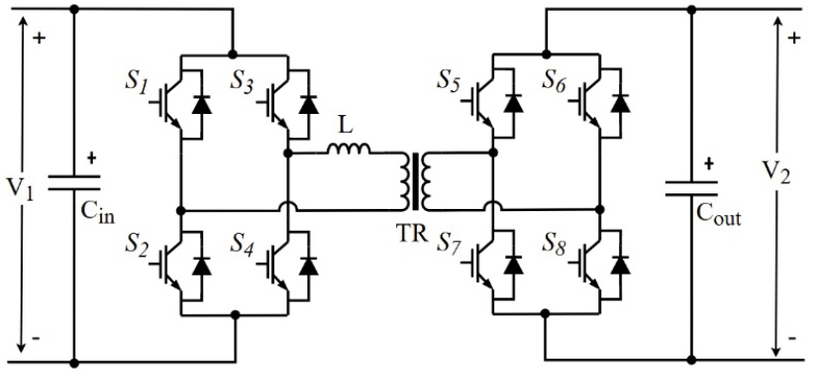

Fig. 6. Topology of the DAB converter.

with a short dead time separating active states. The power flow that the DAB converter transfers (P_{DAB}) depends on the voltages across its ports, switching frequency f, and the series inductance L, and is controlled by the phase shift φ between the gating signals of the active bridges. Equation (2) defines this dependence.

$$P_{\mathrm{DAB}} = \frac{V_1 \cdot V_2 \cdot \varphi(\pi - |\varphi|)}{2 \cdot L \cdot n \cdot f \cdot \pi^2}, \tag{2}$$

where V_1 and V_2 are voltages at the input and output ports of the DAB converter, φ is a phase shift angle between gating signals of the input and output full bridge switching cells (in radians), L is a series inductance connected to the isolation transformer, n is the transformer turns ratio, and f is the switching frequency of transistors $S_1 \ldots S_8$.

2.3. DAB-based PPC – an emerging solution

Unlike the topologies presented above, the DAB-based PPC shown in Fig. 7 does not need to process the full power flowing through the system. One of its ports is connected in parallel with the battery ESS, while the other is connected in series between the battery and the output port, $V_2 = V_1 - V_{\mathrm{Out}}$. As a result, the PPC has to regulate only the voltage difference and, consequently, a fraction of the power defined by the fraction of the voltage regulated by the series port.

Consequently, Eq. (3) could be derived from (2) by redefining voltages to determine the active power processed by the PPC. Analyzing (3), it could be concluded that a smaller voltage difference between the PPC ports results in a lower active power processed. Hence, the efficiency of the DAB stage η_{DAB} has limited influence on the PPC efficiency η_{PPC}, as described by (4).

$$P_{\mathrm{PPC}} = \frac{V_1 \cdot (V_1 - V_{\mathrm{Out}}) \cdot \varphi(\pi - |\varphi|)}{2 \cdot L \cdot n \cdot f \cdot \pi^2}. \tag{3}$$

$$\eta_{\mathrm{PPC}} = \frac{P_{\mathrm{PPC}} - P_{\mathrm{DAB}}(1 - \eta_{\mathrm{DAB}})}{P_{\mathrm{PPC}}} = 1 - K_{pr}(1 - \eta_{\mathrm{DAB}}), \tag{4}$$

where $K_{pr} = P_{\mathrm{DAB}}/P_{\mathrm{PPC}}$ is the partiality ratio. Such a relation allows for low-cost design with generic off-the-shelf components as the DAB stage has reduced influence on the total efficiency of the DAB-based PPC. For example, a PPC designed to process 20% of the total power with a relatively low efficiency of the DAB stage of 90% would still provide 98% of the overall efficiency.

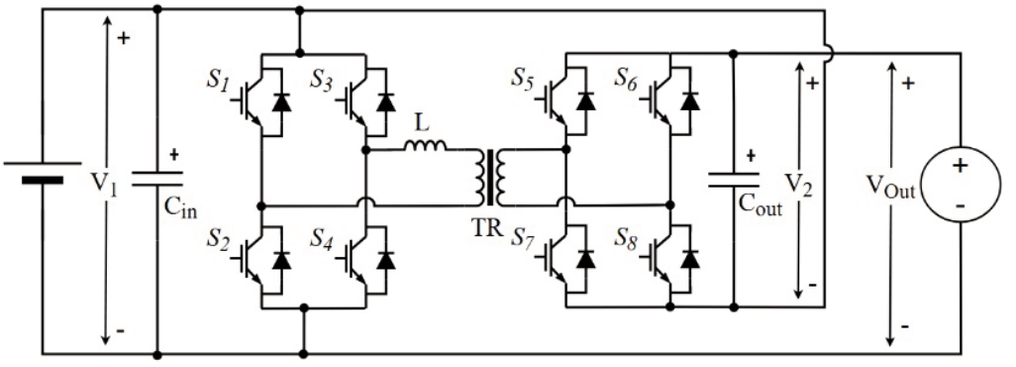

Fig. 7. Topology of the DAB-based PPC.

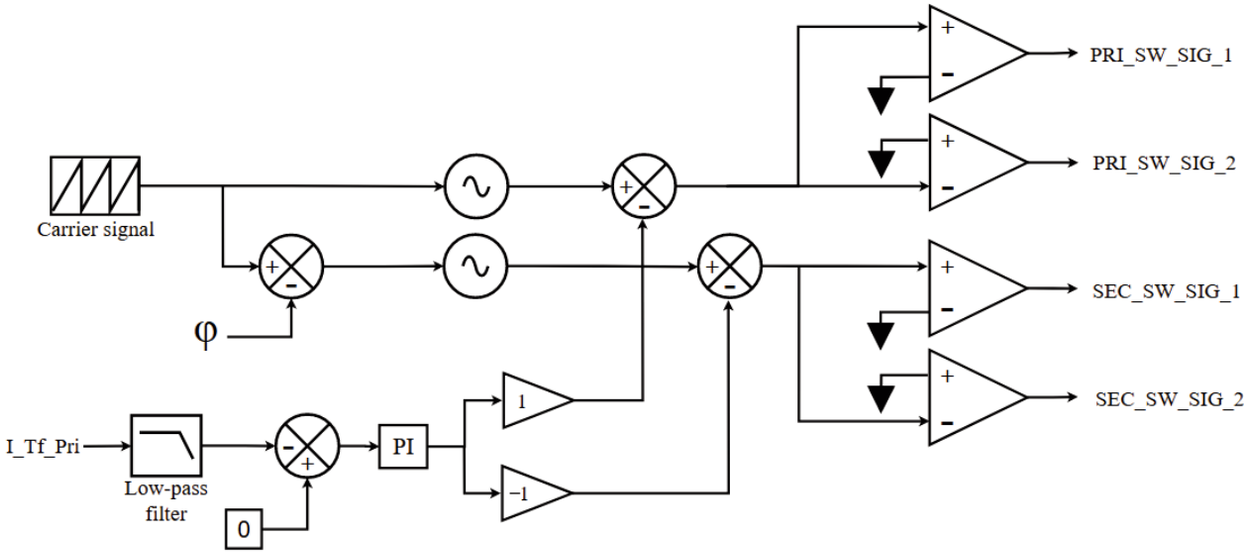

Fig. 8. Generalized modulator for the DAB converter and DAB-based PPC.

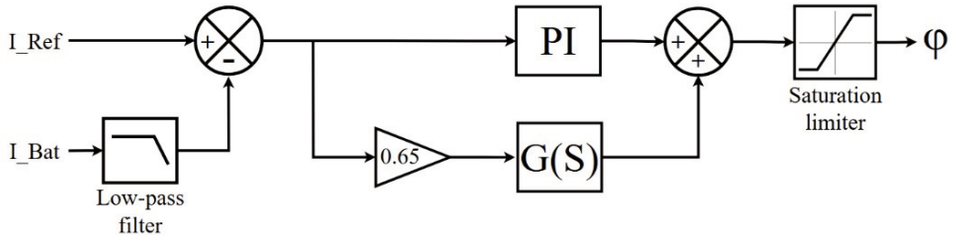

Fig. 9. Generalized PIR controller.

2.4. Unified PIR controller

Unlike the bidirectional half-bridge converter, the DAB converter and the DAB-based PPC require modulation implementation with an additional controller canceling the DC component of the transformer current to avoid its saturation. A generalized structure of a modulator is shown in Fig. 8. The carrier signal defines the switching frequency. Shifting the carrier signal by the normalized phase-shift angle φ allows for implementing phase shift using the sinusoidal control blocks in MATLAB/Simulink. A proportional-integral (PI) controller ensures that the average value of the primary winding transformer current (I_Tf_Pri) remains zero by shifting the generated sinusoidal signals before they are applied to the comparators. As a result, the conventional single phase shift control with DC current compensation is implemented.

As all three converters have to perform the line frequency current ripple rejection, using the same generalized controller design is proposed to ensure fair comparison. As mentioned above, the PIR controller has been proven to perform this task effectively in different applications, including integrating energy sources into an MMC submodule [42–44]. As shown in Fig. 9, the error between the measured (I_Bat) and reference (I_Ref) battery current values is applied to a PI and a resonant controller with outputs connected to the same "Sum" block. The transfer functions of the PI and resonant branches of the controller are defined in Eqs (5) and (6):

$$G_{\mathrm{PI}}(s) = K_p + \frac{K_i}{s}, \tag{5}$$

$$G(s) = \frac{4\pi s}{s^2 + 4\pi s + (2\pi\, 50)^2}, \tag{6}$$

where K_p is the gain of the proportional component, K_i is the gain of the integral component, and $G(s)$ is given for the line frequency of 50 Hz. In the given example, the gain of the resonant branch was empirically set at $K_r = 0.65$.

3. SELECTION OF SIMULATION PARAMETERS AND SIMULATION RESULTS

3.1. Description of the numerical models and case study conditions

All converters were dimensioned for the rated power of 40 kW at the switching frequency of 10 kHz, as presented in Table 1. This power rating of a module allows for good scalability and implementation flexibility of battery ESSs, while the selected switching frequency limits exposure to partial discharges in the given application [49]. It is worth mentioning that the selected capacitances are chosen considering the practical capacity of electrolytic capacitors to operate at a certain high-frequency RMS current, which requires parallel connection of electrolytic capacitors to avoid their overheating [50]. It should be noted that the given values of capacitances are much lower than those needed to decouple the line frequency voltage ripple. Another important observation is that, unlike in a typical single-phase system, this study considers line frequency voltage ripple on the MMC submodule capacitor as the worst-case scenario that could be observed in MMC [51].

All designs consider that the input voltage is always lower than the output voltage, including the influence of the line frequency oscillations. The input inductor of the half-bridge converter was dimensioned for a 5% current ripple in the nominal conditions.

The main difference between the DAB converter and the DAB-based PPC is in the turns ratio of the transformer and the value of the series inductance. The DAB converter has to process the full rated power and match the input and output voltages, while the DAB PPC has to match the input (battery) voltage with the voltage difference between two ports (800 V and 200 V). As the series inductance defines the power transfer capacity of the DAB full power converter and the PPC, these values were selected to limit the phase shift angle to 45 degrees for the DAB converter and 60 degrees for the PPC. These provisions limit reactive power circulating between the transformer windings based on the analysis of the DAB converter's power factor, i.e., the ratio between the active and total apparent power on the transformer, from [52]. The maximum phase shift angle of 45 degrees was selected so the power factor was never below 0.8 to ensure high efficiency of the full power converter. On the other hand, it was assumed that the DAB-based PPC should operate with phase shift angles up to 60 degrees to provide a wider dynamic range of the control variable, which is needed to achieve stable operation in a much wider gain range compared to the full power DAB converter. As a result, the DAB-based PPC could operate with slightly lower power factors (above 0.7), which shall not penalize the PPC's total efficiency as it depends on the efficiency of the DAB cell weakly.

Three models developed in the MATLAB/Simulink environment could be accessed in the TalTech Data Repository to reproduce the case study presented in this section [53]. The corresponding gains of the controllers are also given in Table 1.

To reproduce the operation of each DC-DC converter within an MMC, a case study was synthesized, where the input (battery) voltage was fixed at 800 V, while the output voltage emulated an MMC submodule capacitor with an average voltage of 1000 V and an AC component V_{sm} = 50 V/50 Hz, as shown in Fig. 10a. The battery reference current changes in steps from zero to the maximum positive value of 50 A, followed by a step to the maximum negative value of –50 A, which is later set to zero. This operation emulates the

Table 1. Main parameters used in numerical simulations

Parameter	Converter		
	Half-bridge	DAB	PPC
Nominal input voltage (V)	800		
Nominal output voltage (V)	1000		
Input capacitance (µF)	500	300	300
Output capacitance (µF)	500	200	–
Series port capacitance (µF)	–	–	100
Input inductance (mH)	2	–	–
Leakage/series inductance (µH)	–	80	500
Transformer turns ratio	–	4:5	4:1
Proportional gain K_p	$3 \cdot 10^{-3}$	$5 \cdot 10^{-3}$	$8 \cdot 10^{-3}$
Integral gain K_i	0.1	2	6
Resonant gain K_r	0.1	0.65	0.65
DC current compensation, proportional gain	–	1	1
DC current compensation, integral gain	–	0.1	0.1
Switching frequency (kHz)	10		
Total power (kW)	40		

charging and discharging process of the accelerator magnets at maximum converter power, as shown in Fig. 10b.

Under the given case study conditions, the control variable could be assessed analytically to further validate the experimental results. For example, the solution for the duty cycle of the half-bridge converter D_{hb} under the given conditions could be deducted from (1) and Ohm's law as in (7):

$$D_{hb}(t) = \frac{I_b \cdot R_{eq} + 200 + 50 \cdot \sin(100 \cdot \pi \cdot t)}{1000 + 50 \cdot \sin(100 \cdot \pi \cdot t)}, \tag{7}$$

where t is the time, I_b is the battery current defined in Fig. 10b as a piecewise function, and R_{eq} is the equivalent series resistance that reflects losses in the converter at full power. In the given case, accounting for R_{eq} is important as it significantly influences the control variable. This could be observed from Fig. 11a, where the battery current direction change results in a sizable step in the control variable that directly depends on the R_{eq} value. It is worth mentioning that the control variable is continuous (sinusoidal oscillating within a certain range), as shown in Fig. 11b.

This study uses $R_{eq} = 0.3\ \Omega$ as a practically feasible value for the sake of illustrating converter behavior, which is approximated from the simulation results demonstrated below. Also, the line frequency voltage ripple significantly influences the variations of the control variable. Ideally, the proposed PIR controller has to reproduce a similar behavior of the control variable to ensure a ripple-free battery current.

A similar deduction could be made for the phase shift angle of the DAB converter and the DAB-based PPC, based on (2) and (3), as presented in (8) and (9), correspondingly. Equation (8) is derived from (2) by assuming that $P_{\mathrm{DAB}} = I_b \cdot V_1$, $n = 1.25$, and deducting the equivalent forward voltage drop across R_{eq} from the output voltage for simplicity. A similar derivation could be made for the PPC case when (9) is derived from (3) by assuming $P_{\mathrm{PPC}} = I_b \cdot V_1 \cdot (V_{\mathrm{Out}} - V_1)/(2\ V_1 - V_{\mathrm{Out}})$ and $n = 0.25$, which is easy to show when assuming lossless operation of the DAB-based PPC. Also, observing (8) and (9), a critical design requirement could

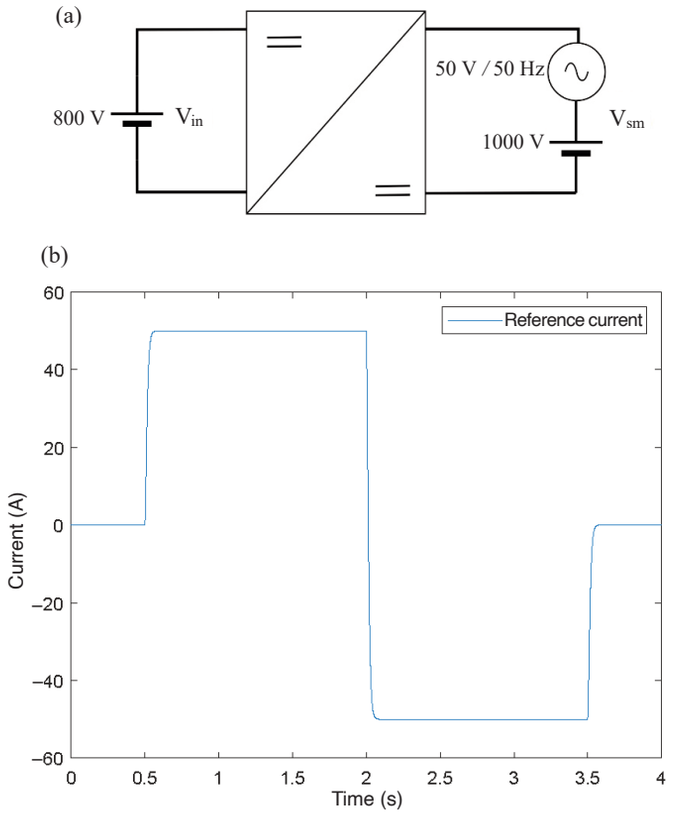

Fig. 10. Case study test conditions: (a) operating voltages and (b) battery reference current.

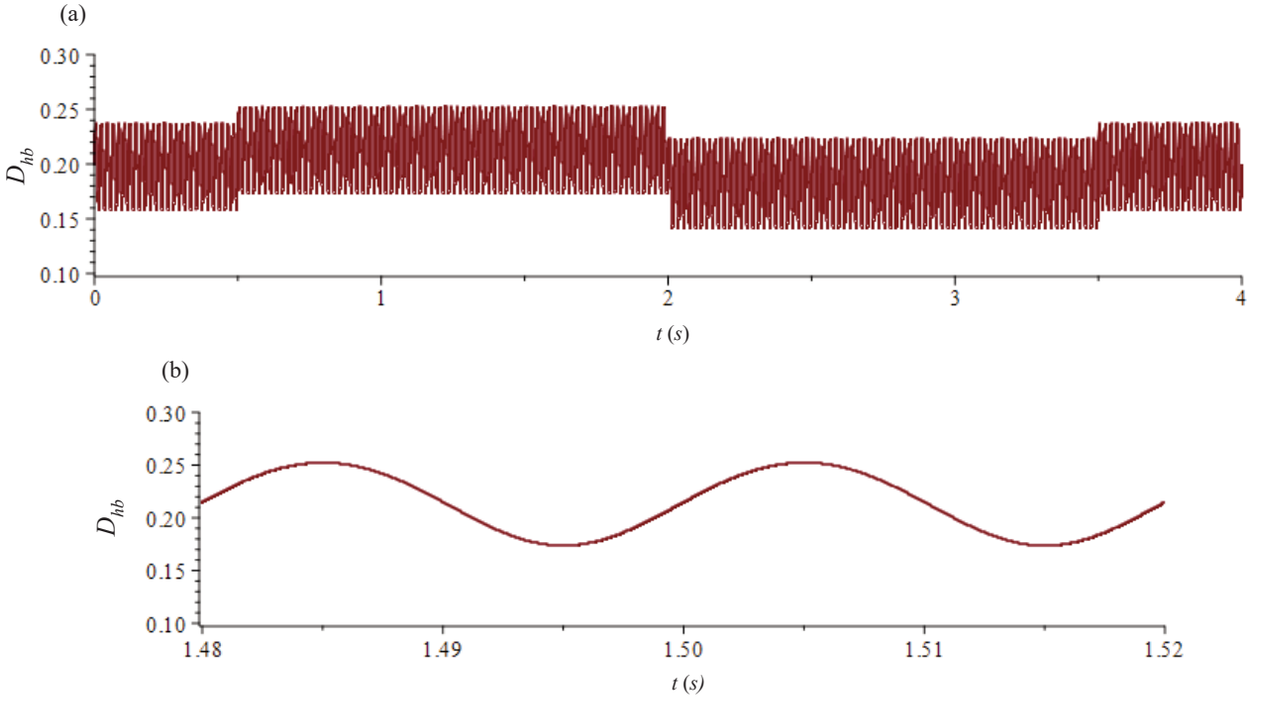

Fig. 11. Control variable of the half-bridge converter estimated for R_{eq} = 0.3 Ω: (a) under the given test conditions, and (b) zoomed section of the waveforms near t = 1.5.

be deducted – the series inductor has to be selected such that the nominator of the fraction under the root sign has to always be below the denominator, including the influence of 50 Hz voltage ripple.

The predicted control variables for the DAB converter and the DAB-based PPC are plotted in Figs 12 and 13, correspondingly, using derivations yielding (8) and (9). It could be observed that the battery current value defines the range of the phase shift, while its sign defines the sign of the phase shift, as predicted. The influence of the equivalent series resistance results in a slight difference between the absolute values of the phase shift when the operation in different power flow directions is closely compared.

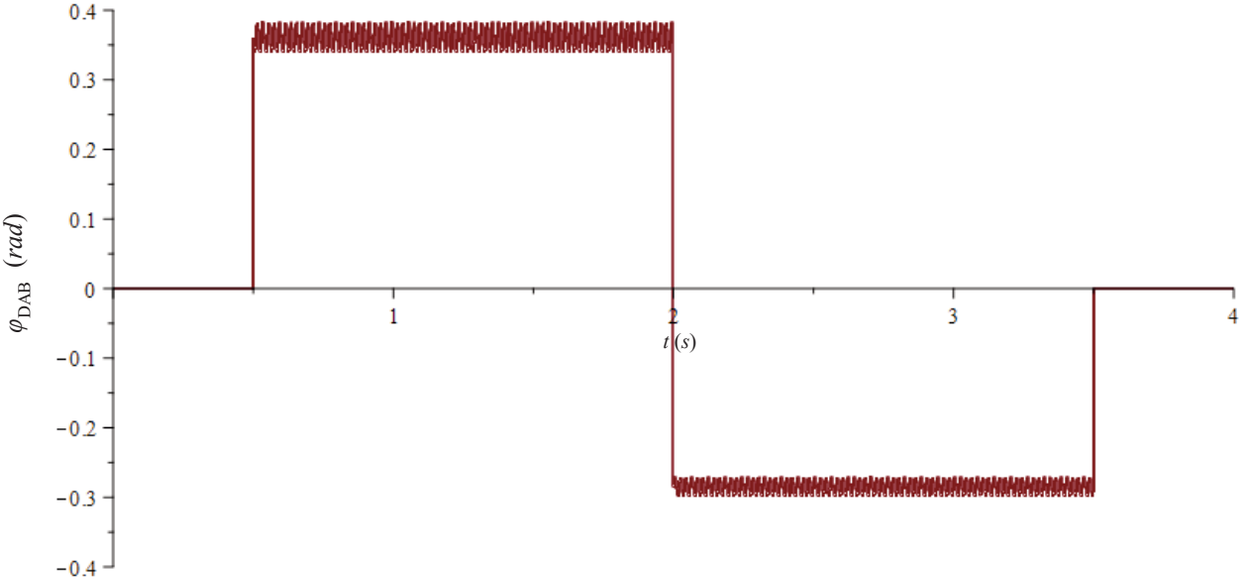

Fig. 12. Control variable of the DAB converter estimated for R_{eq} = 0.3 Ω under the given test conditions.

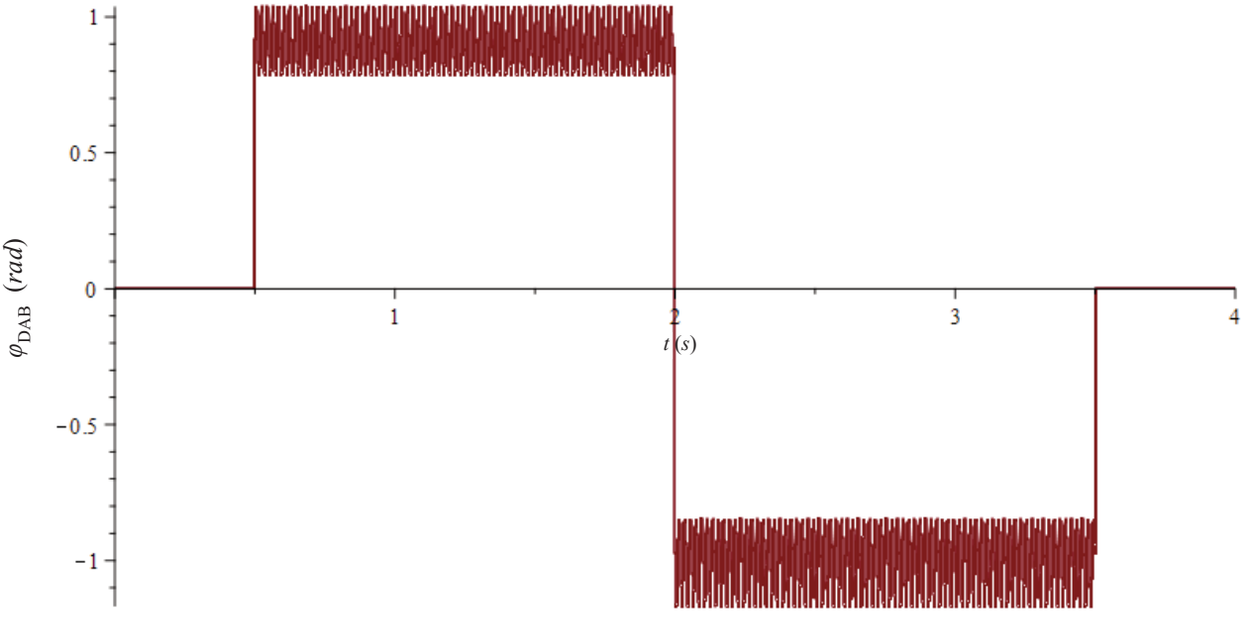

Fig. 13. Control variable of the DAB-based PPC estimated for R_{eq} = 0.3 Ω under the given test conditions.

It could be observed from the derived phase shift equations that the DAB converter and the DAB-based PPC have minor sensitivity to the oscillations of the MMC submodule capacitor voltage and major dependence on the value of the battery current, as could be expected from the DAB operation principle. Also, the phase shift angles of the DAB converter and the DAB-based PPC converge to zero at zero current. In practice, this conclusion could be given only for the DAB converter, as no energy is transferred between its ports. On the other hand, in the case of the PPC, the converter has to continue regulating the series port voltage even at zero current, circulating energy between transformer windings. Such operating conditions could result in high current stress on semiconductor components [29].

$$\varphi_{DAB}(t) = \frac{\pi}{2} \cdot \left(1 - \sqrt{1 - \frac{8 \cdot f \cdot n \cdot L \cdot I_b}{1000 + 50 \cdot \sin(100 \cdot \pi \cdot t) - I_b \cdot R_{eq}}}\right) \text{ for } I_b > 0, \tag{8}$$

$$\varphi_{PPC}(t) = \frac{\pi}{2} \cdot \left(1 - \sqrt{1 - \frac{8 \cdot f \cdot n \cdot L \cdot I_b}{600 - 50 \cdot \sin(100 \cdot \pi \cdot t) + I_b \cdot R_{eq}}}\right) \text{ for } I_b > 0. \tag{9}$$

3.2. Simulation results under case study conditions

Numerical simulations were performed in the MATLAB/Simulink environment. The quality of the battery reference current tracking and the corresponding control variables are presented in Figs 14–16 for the half-bridge converter, DAB converter, and DAB-based PPC, correspondingly.

It could be observed that the half-bridge converter demonstrates the worst reference current tracking performance due to the highest energy stored in its passive components. Also, the duty cycle is continuous in Fig. 14b – it follows a sinusoidal law, as presented above in Fig. 11b. The DC component and magnitude of the sinusoidal signal, i.e., the control variable envelope, change with the battery current, as defined by (7).

Nevertheless, all converters have demonstrated the capability to reject the line frequency ripple from the battery current. The control variables generated by the designed PIR controller are in good agreement with those predicted theoretically in the previous subsection, which validated the correctness of the theoretical derivations presented. Also, virtually complete rejection of the line frequency ripple from the battery current validates the effectiveness of the designed PIR controllers.

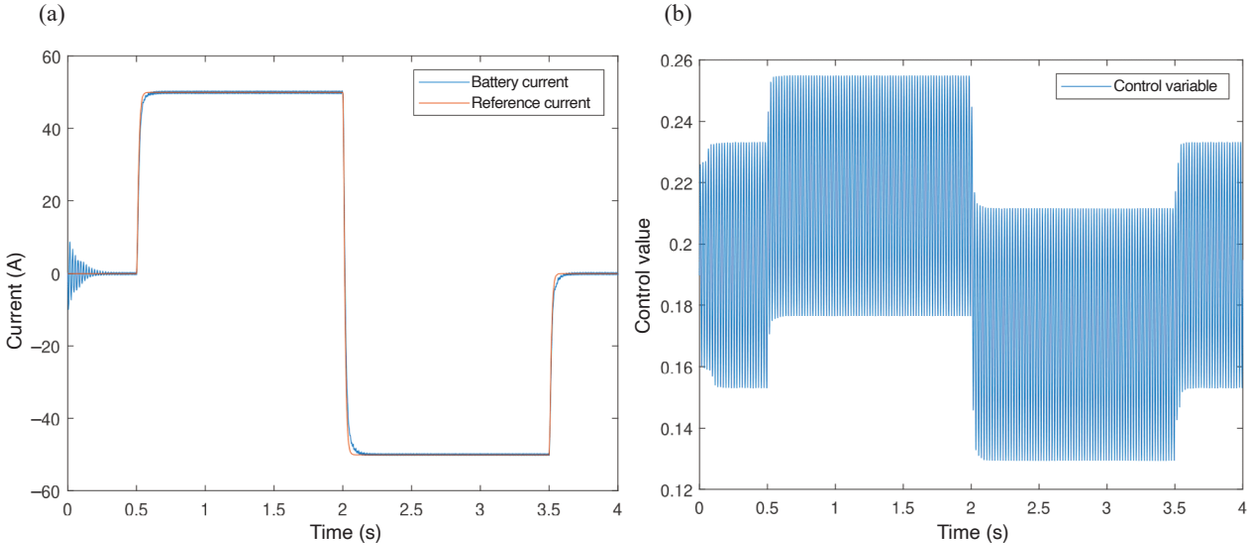

Fig. 14. Simulation results for the half-bridge converter: (a) reference current tracking performance and (b) control variable (S_2 duty cycle).

During simulations, current and voltage waveforms of the main components were recorded and stored to perform virtual prototyping at the next stage.

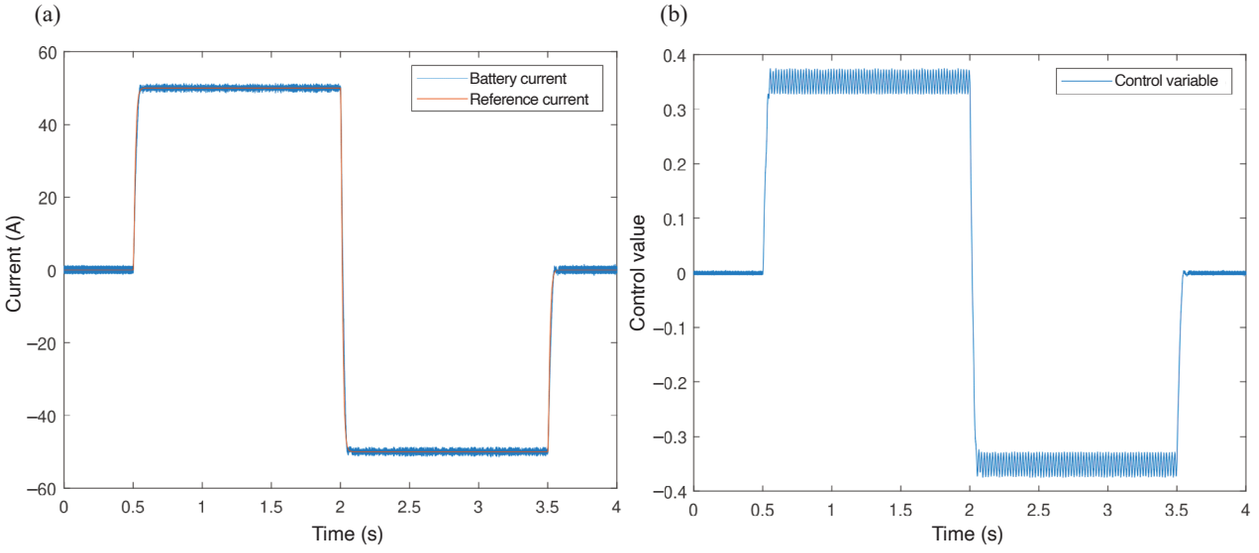

Fig. 15. Simulation results for the DAB converter: (a) reference current tracking performance and (b) control variable (phase shift angle).

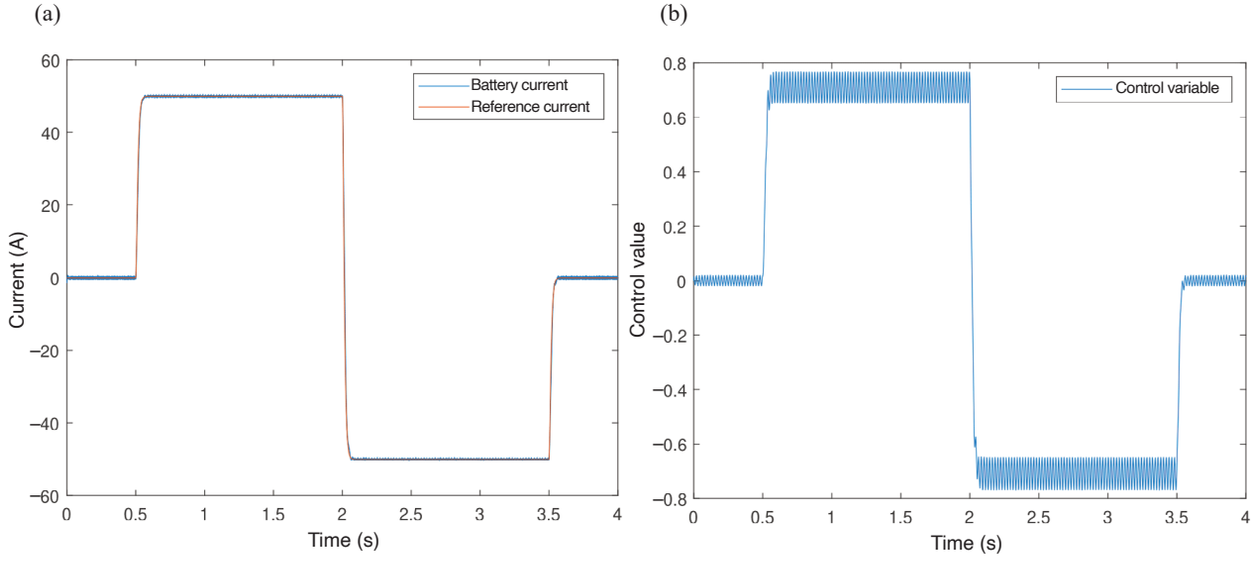

Fig. 16. Simulation results for the DAB-based PPC: (a) reference current tracking performance and (b) control variable (phase shift angle).

4. COMPARISON BASED ON VIRTUAL PROTOTYPING

The real off-the-shelf semiconductor components, capacitors, and active-cooled heatsinks were dimensioned and selected during the virtual prototyping. A preliminary design of magnetic components was performed. This study considered only IGBT power modules as one of the design requirements due to their proven long-term reliability, which is critical for the uninterrupted operation of a particle accelerator. Losses of semiconductor components were calculated based on recorded switching current and voltage and the datasheet curves of turn-on and turn-off losses.

The parameters of the designed magnetic components are listed in Tables 2 and 3. During design, litz wire was considered, enabling us to avoid increasing AC resistance of the winding considerably. Core power loss was deducted based on the volumetric core losses (empirical function of the operating frequency and flux density provided by the manufacturer) resulting from the voltages applied to the windings. DC resistance of the windings was used to calculate copper losses for the magnetic components. As could be expected, the volume of the transformer designed for the DAB converter is much larger than that of the DAB-based PPC due to the much higher operating power. It is assumed that these transformers could be implemented with embedded series inductances to avoid using them as external components prone to possible saturation.

Table 2. Design parameters and virtual prototyping results for transformers

Input design parameters	PPC	DAB
Primary winding voltage (V)	800	800
Secondary winding voltage (V)	200	1000
Nominal power (kW)	10	40
Frequency (kHz)	10	10
Duty cycle	0.5	0.5
Turns ratio	4	0.8
Primary winding RMS current (V)	12.7	55
Secondary winding RMS current (V)	51	45
Core specification	**PPC**	**DAB**
Core manufacturer	Ferroxcube	Ferroxcube
Core material	3C90	3C90
Core shape	E	E
Core size (mm)	100/60/28	100/60/28
Saturation flux density (mT)	470	470
Transformer specification	**PPC**	**DAB**
Primary No. of turns	12	4
Secondary No. of turns	3	5
No. of parallel litz wires in primary winding	1	2
No. of parallel litz wires in secondary winding	3	2
Primary winding strand diameter (cm)	0.0254	0.0254
Secondary winding strand diameter (cm)	0.0254	0.0254
No. of strands in primary winding	400	950
No. of strands in secondary winding	780	610
Fill factor of litz wire	0.28	0.32
No. of stacked cores	4	15
Magnetic inductance in primary winding (mH)	4 ± 25%	1.7 ± 25%
Power loss (W)	56.46	211.73
Volume (L)	1.56	5.88
Flux density swing (mT)	324.36	331.58

During the selection of semiconductor devices and the corresponding active-cooled heatsinks, it was found that the half-bridge converter cannot be implemented using only one power module. Therefore, multidevice implementation shown in Fig. 17a was proposed along with the modulation shown in Fig. 17b. This solution

Table 3. Design parameters and virtual prototyping results for the input inductor in the half-bridge converter

Input design parameters	
Inductance (mH)	2
Core flux density limit (mT)	1400
I_{max} (A)	56
Core manufacturer	MagInc
Core material	Xflux (μ_a = 60)
Core shape	E
Core size (mm)	100/38/39
Saturation flux density (mT)	1600
No. of turns	56
No. of parallel litz wires	1
Fill factor of litz wire	0.55
No. of stacked cores	3
Power loss (W)	66.05
Volume (L)	1.74
Max. magnetic flux density (mT)	866.12

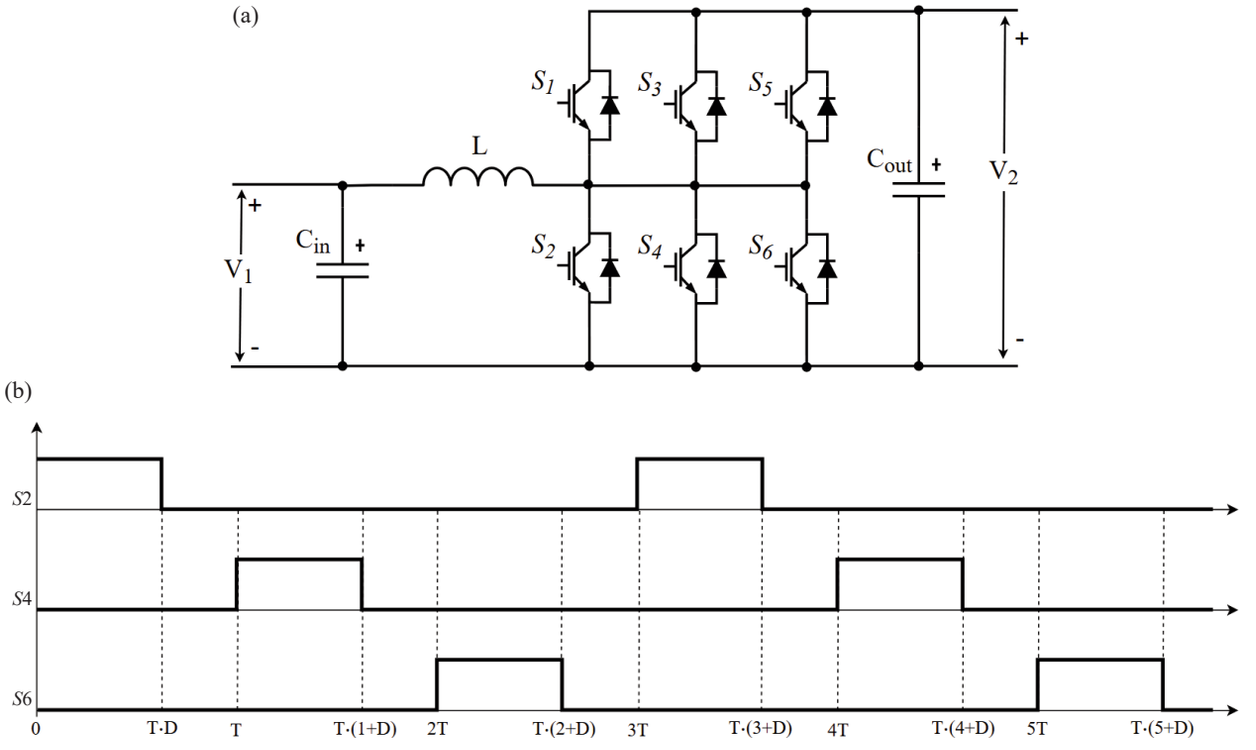

Fig. 17. Multidevice implementation of the half-bridge converter: (a) topology and (b) corresponding modulation given relative to the duration of the switching period T.

Table 4. Main parameters of the designed virtual prototypes

Components and properties	PPC	Half-bridge	DAB
Primary switches	4x 1.2 kV/50 A FF50R12RT4	6x 1.2 kV/150 A FF150R12RT4	4x 1.2 kV/150 A FF150R12RT4
Secondary switches	4x 600 V/200 A FF200R06KE3	–	4x 1.2 kV/150 A FF150R12RT4
Input capacity (μF)	300 (800 V)	500 (800 V)	300 (800 V)
Output capacity (μF)	100 (250 V)	–	200 (1050 V)
DC inductor (μH)	–	2000 (56 A pk)	–
Transformer turns ratio	4:1	–	4:5
Galvanic isolation	No	No	Yes
Switching frequency (kHz)	10	10	10
Power (kW)	40	40	40
Efficiency (%)	98.63	96.30	96.05
Power losses	**PPC**	**Half-bridge**	**DAB**
IGBT conduction losses (W)	176.6	142.4	278.0
IGBT switching losses (W)	361.9	1304.8	1258.3
IGBT total losses (W)	538.6	1444.3	1536.3
Magnetics core losses (W)	8.9	0	36.3
Magnetics copper losses (W)	1.2	37.3	6.58
Other losses (W)	–	–	1.6
Total losses (W)	548.7	1481.6	1579.3
Volume	**PPC**	**Half-bridge**	**DAB**
Magnetics volume (L)	1.57	1.74	5.88
Capacitors volume (L)	0.10	0.32	0.25
Other components volume (L)	0.56	0.27	0.42
Cooling volume (L)	2.18	11.93	7.76
Total volume (L)	4.41	14.26	14.31

Table 5. Cost comparison of the designed virtual prototypes

Item	Cost (€)		
	PPC	Half-bridge	DAB
Custom magnetics	298	320	1079
Capacitors	18.5	32	32.9
IGBT modules	180	210	280
Other filtering	–	–	14
Cooling	615	767	624
Total (€)	1112	1329	2030

allows the converter to distribute its power losses equally among three power modules, making the converter cooling system design feasible [54].

Table 4 presents the main parameters of the final virtual designs of the three converters under study. In these designs, only off-the-shelf components were used when possible. For example, for cooling the DAB converter, heatsink LA-V-7-250-24 (0.048 K/W) and heatsink LA-V-8-300-24 (0.0325 K/W) were used on the primary and secondary sides, respectively. A large heatsink LA-HLV-3-200 (0.02 K/W) was used for the half-bridge converter due to its capability to accommodate three power modules. In the virtual design of the PPC, heatsink LA-28-200-24 (0.12 K/W) and heatsink LA-28-250-24 (0.095 K/W) were used on the primary and secondary sides, respectively. Remarkably, the proposed PPC is not only over three times smaller than the conventional topologies but also cheaper, as shown in the cost comparison given in Table 5. Also, the

PPC efficiency is more than 2% higher than that of the baseline topologies. One of the targets of this study was to build a converter with a total volume of 10 liters or less, which was satisfied only by the PPC technology.

5. CONCLUSIONS

This study has proposed using a DAB-based partial power DC-DC converter to integrate battery energy storage systems into submodules of MMC powering particle accelerator coils. Before this study, this type of converter was not proven capable of line frequency ripple rejection in single-phase applications. This study demonstrates that it is feasible and practical in the case study application. This conclusion is supported by a comprehensive comparison with the conventional non-isolated bidirectional buck/boost half-bridge converter and the isolated DAB converter. The comparison yields that the proposed PPC can provide up to three times higher power density and up to 45% cost reduction. Also, its efficiency is more than 2% higher than the baseline topologies selected for comparison. Hence, particle accelerator applications can benefit from using PPCs. The capital costs of construction can be reduced due to the cost of the PPC being lower than the studied baseline technologies, lower volume reducing the accelerator's cavern excavation needs, and higher efficiency lowering cooling equipment requirements. The operating costs could also be reduced as the entire energy storage system will consume less electricity needed to cover the power loss, and, consequently, the cooling system will consume less. Currently, PPC-based solutions are unavailable on the market and must be developed from scratch.

ACKNOWLEDGMENTS

This research was supported by the Estonian Research Council under the project RVTT3 "CERN Science Consortium of Estonia" and by the Estonian Centre of Excellence in Foundations of the Universe (grant TK202), funded by the Estonian Ministry of Education and Research. The publication costs of this article were partially covered by the Estonian Academy of Sciences.

REFERENCES

1. Brüning, O., Seryi, A. and Verdú-Andrés, S. Electron-hadron colliders: EIC, LHeC and FCC-eh. *Front. Phys.*, 2022, **10**, 88647310, 1–10.
2. Mangano, M. L. (ed.). Physics at the FCC-hh, a 100 TeV pp collider. In *CERN Yellow Reports: Monographs*. CERN, 2017, **3**. https://doi.org/10.23731/CYRM-2017-003
3. Abada, A., Abbrescia, M., AbdusSalam, S. S., Abdyukhanov, I., Abelleira Fernandez, J., Abramov, A. et al. FCC-ee: the lepton collider. *Eur. Phys. J. Spec. Top.*, 2019, **228**(2), 261–623. https://doi.org/10.1140/epjst/e2019-900045-4
4. Blondel, A. and Janot, P. FCC-ee overview: new opportunities create new challenges. *Eur. Phys. J. Plus*, 2022, **137**(1), 92, 1–19.
5. Slettbakk, T. E. *Development of a power quality conditioning system for particle accelerators*. BSc thesis. Norwegian University of Science and Technology, Norway, 2018. https://cds.cern.ch/record/2655157
6. Bouteille, J. F. Power converters for cycling machines. In *Proceedings of the CAS-CERN Accelerator School: Power Converters, Baden, Switzerland, 7–14 May 2014*. CERN, 2015, 171–195. https://doi.org/10.5170/CERN-2015-003.171
7. Burnet, J.-P. Requirements for power converters. In *Proceedings of the CAS-CERN Accelerator School: Power Converters, Baden, Switzerland, 7–14 May 2014*. CERN, 2015, 1–14. https://doi.org/10.5170/CERN-2015-003.1
8. Kahle, K. Power converters and power quality. In *Proceedings of the CAS-CERN Accelerator School: Power Converters, Baden, Switzerland, 7–14 May 2014*. CERN, 2015, 57–82. https://doi.org/10.5170/CERN-2015-003.57
9. Höhn, T. M. *Conceptual power system design for the future circular collider*. PhD thesis. TU Graz, Austria, 2022. https://doi.org/10.3217/MVFD9-7J318
10. Martins, C. Photovoltaic DC injection. Presented at the *I FAST WP11 Annual Meeting, ESS, Lund, Sweden, 3 May 2022*. https://indico.cern.ch/event/1157482

11. Seidel, M. Energy-efficient particle accelerators for research. In *Oxford Research Encyclopedia of Physics*. https://doi.org/10.1093/acrefore/9780190871994.013.137 (accessed 2024-10-15).
12. Colmenero, M., Blanquez, F. R. and Blasco-Gimenez, R. Design concepts for medium voltage DC networks supplying the future circular collider (FCC). In *2022 24th European Conference on Power Electronics and Applications (EPE'22 ECCE Europe), Hanover, Germany, 7–9 September 2022*. IEEE, 2022, 1–11. https://ieeexplore.ieee.org/document/9907266
13. Hohn, T. Advanced power-quality technologies for future circular collider (FCC). Presented at the *4th Annual Meeting of the Future Circular Collider Study, Amsterdam, The Netherlands, 9–13 April 2018*. https://indico.cern.ch/event/656491/contributions/2915665/
14. Yeganeh, M. S. O., Davari, P., Chub, A., Mijatovic, N., Dragičević, T. and Blaabjerg, F. A single-phase reduced component count asymmetrical multilevel inverter topology. *IEEE J. Emerg. Sel. Topics Power Electron.*, 2021, **9**(6), 6780–6790. https://doi.org/10.1109/JESTPE.2021.3066396
15. Colmenero, M., Blanquez, F. R. and Blasco-Gimenez, R. DC powering solutions for the future circular collider: converter topologies, protection, and control. *IEEE Open J. Ind. Electron.*, 2023, **4**, 694–708. https://doi.org/10.1109/OJIES.2023.3336981
16. Moratalla, M. C., Vidal-Albalate, R., Delgado, F. R. B. and Blasco-Gimenez, R. Fault-tolerant strategies in MMC-based high power magnet supply for particle accelerator. *Math. Comput. Simul.*, 2024, **224**(P A), 63–79. https://doi.org/10.1016/j.matcom.2023.07.014
17. Chen, Q., Li, R. and Cai, X. Analysis and fault control of hybrid modular multilevel converter with integrated battery energy storage system. *IEEE J. Emerg. Sel. Topics Power Electron.*, 2017, **5**(1), 64–78. https://doi.org/10.1109/JESTPE.2016.2623672
18. Barresi, M., Ferri, E. and Piegari, L. An MMC-based fully modular ultra-fast charging station integrating a battery energy storage system. In *2022 IEEE 16th International Conference on Compatibility, Power Electronics, and Power Engineering (CPE-POWERENG), Birmingham, United Kingdom, 29 June–1 July 2022*. IEEE, 2022, 1–8. https://doi.org/10.1109/CPE-POWERENG54966.2022.9880885
19. Ma, Y., Xiao, J., Lin, H. and Wang, Z. A novel battery integration method of modular multilevel converter with battery energy storage system for capacitor voltage ripple reduction. *IEEE Trans. Ind. Electron.*, 2021, **68**(12), 12250–12261. https://doi.org/10.1109/TIE.2020.3044780
20. Abada, A., Abbrescia, M., AbdusSalam, S. S., Abdyukhanov, I., Abelleira Fernandez, J., Abramov, A. et al. FCC-hh: the hadron collider. *Eur. Phys. J. Spec. Top.*, 2019, **228**(4), 755–1107. https://doi.org/10.1140/epjst/e2019-900087-0
21. Mohseni, P., Husev, O., Vinnikov, D., Strzelecki, R., Romero-Cadaval, E. and Tokarski, I. Battery technologies in electric vehicles: improvements in electric battery packs. *IEEE Ind. Electron. Mag.*, 2023, **17**(4), 55–65. https://doi.org/10.1109/mie.2023.3252265
22. Stynski, S., Luo, W., Chub, A., Franquelo, L. G., Malinowski, M. and Vinnikov, D. Utility-scale energy storage systems: converters and control. *IEEE Ind. Electron. Mag.*, 2020, **14**(4), 32–52. https://doi.org/10.1109/MIE.2020.3011655
23. Schroeder, M., Henninger, S., Jaeger, J., Raš, A., Rubenbauer, H. and Leu, H. Integration of batteries into a modular multilevel converter. In *2013 15th European Conference on Power Electronics and Applications (EPE), Lille, France, 2–6 September 2013*. IEEE, 2013, 1–12. https://doi.org/10.1109/EPE.2013.6634328
24. Wang, Z., Lin, H., Ma, Y. and Wang, T. A prototype of modular multilevel converter with integrated battery energy storage. In *2017 IEEE Applied Power Electronics Conference and Exposition (APEC), Tampa, FL, USA, 26–30 March 2017*. IEEE, 2017, 434–439. https://doi.org/10.1109/APEC.2017.7930730
25. Soong, T. and Lehn, P. W. Evaluation of emerging modular multilevel converters for BESS applications. *IEEE Trans. Power Deliv.*, 2014, **29**(5), 2086–2094. https://doi.org/10.1109/TPWRD.2014.2341181
26. Debnath, S., Qin, J., Bahrani, B., Saeedifard, M. and Barbosa, P. Operation, control, and applications of the modular multilevel converter: a review. *IEEE Trans. Power Electron.*, 2015, **30**(1), 37–53. https://doi.org/10.1109/TPEL.2014.2309937
27. Anzola, J., Aizpuru, I., Romero, A. A., Loiti, A. A., Lopez-Erauskin, R. and Artal-Sevil, J. S. Review of architectures based on partial power processing for DC-DC applications. *IEEE Access*, 2020, **8**, 103405–103418. https://doi.org/10.1109/ACCESS.2020.2999062
28. Chub, A., Hassanpour, N., Yadav, N., Jalakas, T., Blinov, A. and Vinnikov, D. Analysis of design requirements and optimization possibilities of partial power converter for photovoltaic string applications in DC microgrids. *IEEE Access*, 2024, **12**, 14605–14619. https://doi.org/10.1109/ACCESS.2024.3354375
29. Hassanpour, N., Chub, A., Blinov, A. and Vinnikov, D. Soft-switching bidirectional step-up/down partial power converter with reduced components stress. *IEEE Trans. Power Electron.*, 2023, **38**(11), 14166–14177. https://doi.org/10.1109/TPEL.2023.3289061
30. dos Santos, N. G. F., Zientarski, J. R. R. and da Silva Martins, M. L. A review of series-connected partial power converters for DC–DC applications. *IEEE J. Emerg. Sel. Topics Power Electron.*, 2022, **10**(6), 7825–7838. https://doi.org/10.1109/JESTPE.2021.3082869
31. Artal-Sevil, J. S., Anzola, J., Ballestín-Bernad, V. and Bernal-Agustín, J. L. Analysis and implementation of different non-isolated partial-power processing architectures based on the Cuk converter. In *Proceedings of the 2022 24th European Conference on Power Electronics and Applications (EPE'22 ECCE Europe), Hanover, Germany, 7–9 September 2022*. IEEE, 2022, 1–10.
32. Anzola, J., Aizpuru, I., Arruti, A., Artal-Sevil, J. S. and Bernal, C. Demystifying non-isolated DC-DC topologies on partial power processing architectures. *Electronics*, 2022, **11**(3), 480. https://doi.org/10.3390/electronics11030480

33. Purgat, P., Shekhar, A., Qin, Z. and Bauer, P. Low-voltage dc system building blocks: integrated power flow control and short circuit protection. *IEEE Ind. Electron. Mag.*, 2023 **17**(1), 6–20. https://doi.org/10.1109/MIE.2021.3106275
34. Purgat, P., van der Blij, N. H., Qin, Z. and Bauer, P. Partially rated power flow control converter modeling for low-voltage DC grids. *IEEE J. Emerg. Sel. Topics Power Electron.*, 2020, **8**(3), 2430–2444. https://doi.org/10.1109/JESTPE.2019.2915166
35. Müller, N., Kouro, S., Zanchetta, P. and Wheeler, P. Bidirectional partial power converter interface for energy storage systems to provide peak shaving in grid-tied PV plants. In *2018 IEEE International Conference on Industrial Technology (ICIT), Lyon, France, 20–22 February 2018*. IEEE, 2018, 892–897. https://doi.org/10.1109/ICIT.2018.8352296
36. Mishra, S., Tamballa, S., Pallantala, M., Raju, S. and Mohan, N. Cascaded dual-active bridge cell based partial power converter for battery emulation. In *2019 20th Workshop on Control and Modeling for Power Electronics (COMPEL), Toronto, ON, Canada, 17–20 June 2019.* IEEE, 2019, 1–7. https://doi.org/10.1109/COMPEL.2019.8769712
37. Iyer, V. M., Gulur, S., Bhattacharya, S. and Ramabhadran, R. A partial power converter interface for battery energy storage integration with a DC microgrid. In *2019 IEEE Energy Conversion Congress and Exposition (ECCE), Baltimore, MD, USA, 29 September – 3 October 2019*. IEEE, 2019, 5783–5790. https://doi.org/10.1109/ECCE.2019.8912590
38. Mira, M. C., Zhang, Z., Jørgensen, K. L. and Andersen, M. A. E. Fractional charging converter with high efficiency and low cost for electrochemical energy storage devices. *IEEE Trans. Ind. Appl.*, 2019, **55**(6), 7461–7470. https://doi.org/10.1109/TIA.2019.2921295
39. Viinamäki, J., Jokipii, J. and Suntio, T. Improving double-line-frequency voltage ripple rejection capability of DC/DC converter in grid connected two-stage PV inverter using DC-link voltage feedforward. In *2016 18th European Conference on Power Electronics and Applications (EPE'16 ECCE Europe), Karlsruhe, Germany, 5–9 September 2016.* IEEE, 2016, 1–10. https://doi.org/10.1109/EPE.2016.7695539
40. Hu, X., Shao, W., Cheng, Y., Zhang, C. and Han, Y. Research on ADRC controller of bidirectional DC-DC converter for MMC-BESS. *Energy Rep.*, 2023, **9**, 1627–1636. https://doi.org/10.1016/j.egyr.2023.04.175
41. Zhao, X., Zhang, L., Born, R. and Lai, J.-S. Solution of input double-line frequency ripple rejection for high-efficiency high-power density string inverter in photovoltaic application. In *2016 IEEE Applied Power Electronics Conference and Exposition (APEC), Long Beach, CA, USA, 20–24 March 2016*. IEEE, 2016, 1148–1154. https://doi.org/10.1109/APEC.2016.7468014
42. Yang, S., Zhuang, F., Wang, Y., Tang, Y. and Wang, P. Low-frequency voltage ripple suppression for MMCs with split-capacitor submodules. *IEEE Trans. Power Electron.*, 2024, **39**(1), 483–492. https://doi.org/10.1109/TPEL.2023.3327036
43. Liu, C., Wang, J., Colombage, K., Gould, C., Sen, B. and Stone, D. Current ripple reduction in 4kW LLC resonant converter based battery charger for electric vehicles. In *2015 IEEE Energy Conversion Congress and Exposition (ECCE), Montreal, QC, Canada, 20–24 September 2015*. IEEE, 2015, 6014–6021. https://doi.org/10.1109/ECCE.2015.7310503
44. Fawzi, M., Abdelsalam, I., Aboushady, A. A. and Abdel Maksoud, S. A. A modified phase shift control of the dual active bridge-based modular power electronic transformer to minimize the LVdc side voltage ripples under unbalanced load conditions. *IEEE Access*, 2022, **10**, 81309–81322. https://doi.org/10.1109/ACCESS.2022.3195941
45. Vasiladiotis, M. and Rufer, A. Analysis and control of modular multilevel converters with integrated battery energy storage. *IEEE Trans Power Electron.*, 2015, **30**(1), 163–175. https://doi.org/10.1109/TPEL.2014.2303297
46. Shao, S., Chen, L., Shan, Z., Gao, F., Chen, H. and Sha, D. Modeling and advanced control of dual-active-bridge DC–DC converters: a review. *IEEE Trans. Power Electron.*, 2022, **37**(2), 1524–1547. https://doi.org/10.1109/TPEL.2021.3108157
47. Bayat, H. and Yazdani, A. A hybrid MMC-based photovoltaic and battery energy storage system. *IEEE Power Energy Technol. Syst. J.*, 2019, **6**(1), 32–40. https://doi.org/10.1109/JPETS.2019.2892418
48. Zhao, B., Song, Q., Liu, W. and Sun, Y. Overview of dual-active-bridge isolated bidirectional DC–DC converter for high-frequency-link power-conversion system. *IEEE Trans. Power Electron.*, 2014, **29**(8), 4091–4106. https://doi.org/10.1109/TPEL.2013.2289913
49. Jiang, J., Zhang, B., Li, Z., Ranjan, P., Chen, J. and Zhang, C. Partial discharge features for power electronic transformers under high-frequency pulse voltage. *IEEE Trans. Plasma Sci.*, 2021, **49**(2), 845–853. https://doi.org/10.1109/TPS.2021.3053960
50. Liivik, E., Vinnikov, D., Chub, A., Shen, Y., Wang, H. and Blaabjerg, F. Reliability study of input side capacitors in impedance-source PV microconverters. In *IECON 2019 – 45th Annual Conference of the IEEE Industrial Electronics Society, Lisbon, Portugal, 14–17 October 2019*. IEEE, 2019, 5026–5032. https://doi.org/10.1109/IECON.2019.8927173
51. Merlin, M. M. C. and Green, T. C. Cell capacitor sizing in multilevel converters: cases of the modular multilevel converter and alternate arm converter. *IET Power Electron.*, 2015, **8**(3), 350–360. https://doi.org/10.1049/iet-pel.2014.0328
52. Gitau, M. N., Ebersohn, G. and Kettleborough, J. G. Power processor for interfacing battery storage system to 725V DC bus. *Energy Convers. Manag.*, 2007, **48**(3), 871–881. https://doi.org/10.1016/j.enconman.2006.08.019
53. Niinemägi, J. Simulink simulation models of three different power converters. *TalTech Data Repository*, 2023. https://doi.org/10.48726/ws4hc-q3b07
54. Hegazy, O., Mierlo, J. V. and Lataire, P. Analysis, modeling, and implementation of a multidevice interleaved DC/DC converter for fuel cell hybrid electric vehicles. *IEEE Trans. Power Electron.*, 2012, **27**(11), 4445–4458. https://doi.org/10.1109/TPEL.2012.2183148

Aku energiasalvestit tuleviku ringpõrguti energiasüsteemiga ühendava osavõimsusmuunduri võrdlev teostatavusuuring

Andrii Chub, Joosep Niinemägi, Manuel Colmenero ja Davide Aguglia

Hiljuti välja töötatud osavõimsusmuundurid on ilmutanud potentsiaali suurendada märgatavalt jõuelektroonikasüsteemide tõhusust ja võimsustihedust, kuid seni ei ole nende teostatavust erinevates rakendustes piisavalt uuritud. Artiklis käsitletakse kaksikaktiivsild-topoloogial põhineva osavõimsusmuunduri sobivust ja jõudlust aku integreerimiseks osakeste kiirendi magneteid toitvasse modulaarsesse mitmetasandilisse muundurisse. Simulatsiooni tulemused tõestavad, et osavõimsusmuundur suudab tõrjuda aku poolel võrgusageduslikku pulsatsiooni ja juhtida voolu piisava dünaamikaga. Võrdlus tüüpiliste alalispinge topoloogiatega lubab väiksemat maksumust ning suuremat efektiivsust ja võimsustihedust. Tulemused põhinevad MATLAB/Simulinki simulatsioonidel ja virtuaalsel prototüüpimisel, mis tugineb saadaolevatele valmiskomponentidele.